Phonon coherence and minimum thermal conductivity in disordered superlattice

Xin Wu,[1] Zhang Wu,[2] Ting Liang,[3] Zheyong Fan,[4, *] Jianbin Xu,[3] Masahiro Nomura,[1, †] and Penghua Ying[5, ‡]

[1]*Institute of Industrial Science, The University of Tokyo, Tokyo 153-8505, Japan*
[2]*AVIC Jiangxi Hongdu Aviation Industry Group Company Ltd., Nanchang 330024, P. R. China*
[3]*Department of Electronic Engineering and Materials Science and Technology Research Center,*
The Chinese University of Hong Kong, Shatin, N.T., Hong Kong SAR, 999077, P. R. China
[4]*College of Physical Science and Technology, Bohai University, Jinzhou 121013, P. R. China*
[5]*Department of Physical Chemistry, School of Chemistry, Tel Aviv University, Tel Aviv, 6997801, Israel*
(Dated: October 3, 2024)

Phonon coherence elucidates the propagation and interaction of phonon quantum states within superlattice, unveiling the wave-like nature and collective behaviors of phonons. Taking $MoSe_2$/WSe_2 lateral heterostructures as a model system, we demonstrate that the intricate interplay between wave-like and particle-like phonons, previously observed in perfect superlattice only, also occurs in disordered superlattice. By employing molecular dynamics simulation based on a highly accurate and efficient machine-learned potential constructed herein, we observe a non-monotonic dependence of the lattice thermal conductivity on the interface density in both perfect and disordered superlattice, with a global minimum occurring at relatively higher interface density for disordered superlattice. The counter-intuitive phonon coherence contribution can be characterized by the lagged self-similarity of the structural sequences in the disordered superlattice. Our findings extend the realm of coherent phonon transport from perfect superlattice to more general structures, which offers more flexibility in tuning thermal transport in superlattices.

I. INTRODUCTION

Phonon thermal transport exhibits significant potential in nanoscale thermal physics, especially in semiconductors and insulators where the lattice thermal conductivity (LTC) is almost entirely derived from lattice vibrations [1]. As the quanta of lattice vibrations, phonons exhibit particle-like behavior through energy quantization and quasi-particle interactions, playing a crucial role in thermal transport by affecting LTC through scattering and collision processes. However, the wave nature of phonons is equally significant [2, 3]. It describes the characteristics of lattice vibrations through the relationship between wave vector and frequency, manifesting as dispersion relations in wave equations. By controlling phonon wave vectors and frequencies, one can influence phonon propagation paths and scattering mechanisms. For instance, when the phonon wavelength is comparable to the characteristic dimensions of a material, phonon transport exhibits significant coherence [4–10]. This means phonons can travel coherently without losing phase information, thereby significantly altering the LTC and thermal transport properties of the material.

In periodically alternating nanostructures known as superlattices, composed of two or more different materials, phonons experience multiple reflections and interference at periodic interfaces, leading to the formation of new phonon spectra and coherent transport [4, 11]. The wave nature of phonons becomes critically important. Perfect superlattices provide an ideal platform to explore and utilize the coherent transport properties of phonons [12–14]. This behavior has been theoretically predicted and experimentally verified in various systems, from semiconductors such as GaAs/AlAs [6, 12] to two-dimensional (2D) materials like graphene/h-BN [8, 9, 15]. However, disordered superlattices offer complex interface scattering and localization effects, making them ideal systems to contrast with perfect superlattices. These structures are often used to verify phonon coherence in superlattices but have not received equivalent attention or treatment in their own right and remain elusive.

For predicting the properties of new structures and materials, molecular dynamics (MD) simulation is an excellent choice, which can implicitly include all orders of lattice anharmonicity and phonon scattering and provide detailed atomic-level information [16]. It circumvents the limitations of Boltzmann transport equation (BTE) in describing higher-order phonon scattering and in handling complex systems with large unitcells. Additionally, machine-learned potential (MLP) [17] offers high-precision descriptions of interatomic interactions, providing excellent descriptions for thermal transport in many materials [18–22].

In this work, we developed a MLP based on the neuroevolution potential (NEP) framework [23–25] and used nearly lattice-matched 2D $MoSe_2$/WSe_2 (2H-phase) lateral heterostructures as the model systems. We investigated the LTC of perfect and disordered superlattices at room temperature with various interface densities. Detailed analyses of the spectral LTC elucidate the origins of two distinct minimum thermal conductivities in perfect and disordered superlattices. We also established a factor of disorder to describe the LTC trends in disordered superlattices and revealed the LTC variations

* brucenju@gmail.com
† nomura@iis.u-tokyo.ac.jp
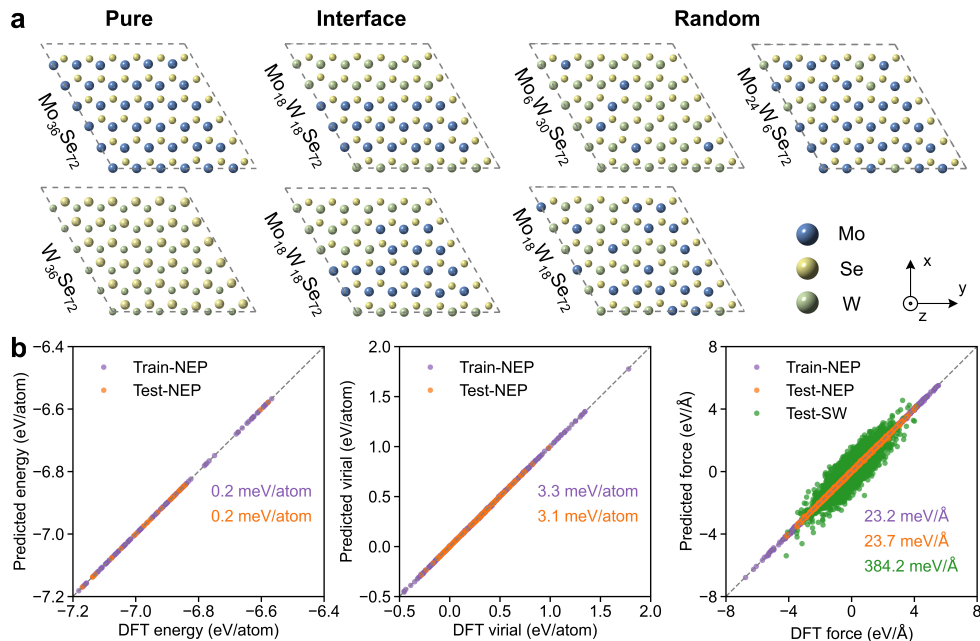‡ hityingph@tauex.tau,ac.il

FIG. 1. The construction of NEP model. (a) The cells of the reference structures, including pure MoSe$_2$, pure WSe$_2$, and their heterostructures. (b) The energy, virial, and force calculated from the NEP model and the SW potential compared to the DFT reference data.

in the coherent transport regime of perfect superlattices through phonon band folding.

II. RESULTS AND DISCUSSIONS

A. NEP model evaluation

We employed the NEP approach [23–25] (see section IV C for details) to train a MLP for MoSe$_2$/WSe$_2$ lateral heterostructures against the total energy, atomic forces, and virials of a training dataset from density functional theory (DFT) calculations (see section IV B for details). As shown in Figure 2(a), the training dataset includes pure MX$_2$ structures, their lateral heterostructures with both flat and embedded interfaces, and random ternary Mo$_x$W$_{1-x}$Se structures (see section IV A for details).

As depicted in Figure 1(b), the NEP model achieves high accuracy in both training and test datasets, with root mean square errors (RMSEs) of energy, virial, and force below 0.5 meV/atom, 3.3 meV/atom, and 23.7 meV/Å, respectively. For comparison, we evaluated the atomic forces predicted by a Stillinger-Weber (SW) potential [39] against DFT results and found that its RMSE (384.2 meV/Å) is an order of magnitude higher. In terms of computational efficiency, on a single GeForce RTX 4090 graphic processing units (GPU), the present NEP model can achieve 2.4 × 10^7 atom-steps per second as implemented in GPUMD.[25] This performance is comparable to the speed of the traditional SW potential implemented in LAMMPS [40], which achieves 5.8 × 10^7 atom-step per second using 64 Xeon Platinum 9242 CPU cores.

After obtaining the NEP model, we verified its accuracy by comparing the predicted phonon dispersion and LTC of MoSe$_2$ and WSe$_2$ with results from DFT, SW, as well as experimental measurement. As shown in Figure 2(a), the phonon dispersion curves predicted by the NEP model align perfectly with DFT, providing a much more accurate band gap for both MoSe$_2$ and WSe$_2$ compared to the SW potential [41]. For the LTC predictions for monolayer MoSe$_2$ and WSe$_2$ (see Figure 2(d)), our NEP-based homogeneous non-equilibrium molecular dynamics (HNEMD) results (see section IV D for details) closely match experimental measurements [27–29], whereas SW-driven MD simulations [35–38] significantly underestimate the LTCs, aligning more with measured LTC of bulk MoSe$_2$ and WSe$_2$ [26]. The BTE-anharmonic lattice dynamics (ALD) predictions [30–34] based on DFT force constants (labeled as "DFT" in Figure 2(b)) exhibit large variations and less satisfactory alignment to experimental results than the predictions from NEP.

B. The model lateral heterostructures

As shown in Figure 3, we chose MoSe$_2$ and WSe$_2$ to form a binary model system, both in the 2H phase. The

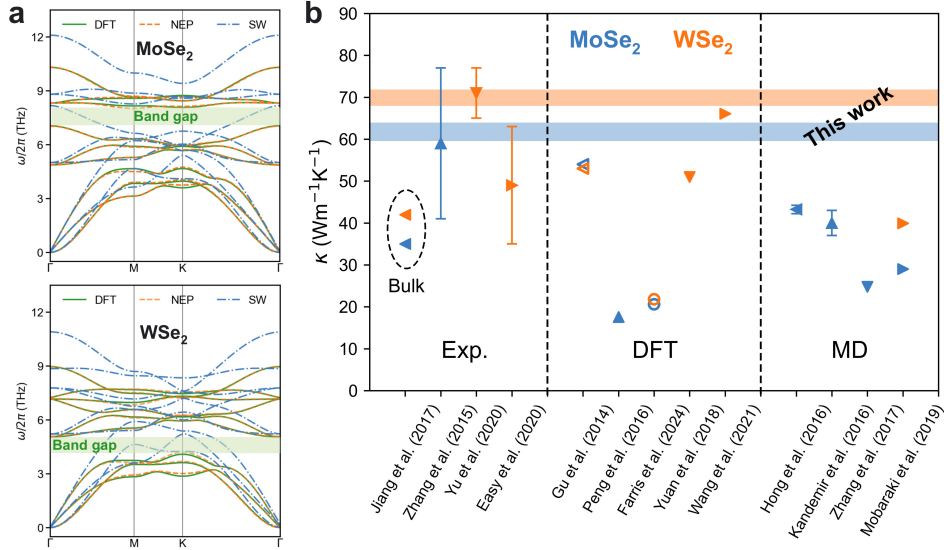FIG. 2. Benchmark of the accuracy of the NEP model for $MoSe_2$ and WSe_2. (a) The phonon dispersion relations of $MoSe_2$ and WSe_2 calculated by DFT, the NEP model, and the SW potential. (b) Comparison of LTC of monolayer $MoSe_2$ and WSe_2 with respect to other experimental [26–29], DFT-based [30–34], and SW-based MD [35–38] results at the room temperature. The two horizontal bands are the results with error bars from this work by NEP-based MD, which show good agreement with the experiments.
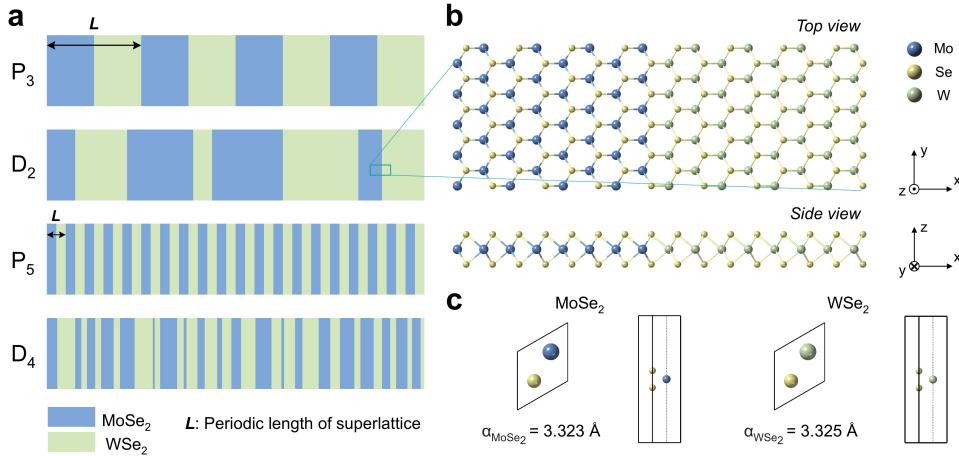

FIG. 3. Illustration of $MoSe_2$/WSe_2 lateral heterostructures. (a) Two pairs of $MoSe_2$/WSe_2 lateral heterostructures, each consisting of a perfect (P) and a disordered (D) superlattice with equal interface density: P_3 paired with D_2, and P_5 paired with D_4. L denotes the periodic length of the superlattice. (b) Local atomic-level zoomed-in view of the $MoSe_2$/WSe_2 heterostructure interface. (c) The unit cell of $MoSe_2$ and WSe_2 and their lattice constants.

optimized lattice constant from DFT (NEP) are 3.323 Å and 3.325 Å(3.321 Å and 3.321 Å) for $MoSe_2$ and WSe_2, respectively, resulting in a negligible lattice mismatch. Notably, a monolayer $MoSe_2$/WSe_2 lateral heterostructure was recently synthesized and found to exhibit electrical rectification [42].

The lateral heterostructures here include two types: eight perfect superlattices (labeled as $P_1 \sim P_8$) and ten disordered superlattices (labeled as $D_1 \sim D_{10}$). For each superlattice, we define the interface density as the number of heterointerfaces per unit lateral length. This definition allows for a clear correspondence between perfect and disordered superlattices. The structural parameters of considered superlattices are listed in Table I, and Figure 3(a) presents the sequences of two pairs of perfect and disordered superlattices (P_3 and D_2, P_5 and D_4) with identical interface density. For a disordered superlattice with the specified interface density, we generate the corresponding configurations using genetic algorithms [43] under a constraint of $MoSe_2$:WSe_2 = 1:1. In this case,

TABLE I. The $MoSe_2/WSe_2$ perfect and disordered superlattice with different interface densities considered in this work. The fourth column, L denotes the periodic length of the superlattice (see Figure 3(a))

Interface density (nm^{-1})	Perfect	Disordered	L (nm)
0.0351	P_1	N/A	56.9500
0.0702	P_2	D_1	28.4750
0.1405	P_3	D_2	14.2370
0.3512	P_4	D_3	5.6950
0.7024	P_5	D_4	2.8470
0.8780	P_6	D_5	2.2780
1.2291	N/A	D_6	N/A
1.7559	P_7	D_7	1.1390
2.1071	N/A	D_8	N/A
2.6339	N/A	D_9	N/A
3.1607	N/A	D_{10}	N/A
3.5119	P_8	N/A	0.5695

the difference between perfect and disordered superlattices with the same interface density lies solely in the varying positions of the heterointerfaces.

One should note that for perfect superlattices, P_1 and P_8, which have the largest and smallest periodic lengths (see Table I) respectively, there are no corresponding disordered counterparts. In the case of P_1, with minimal interface density and only a single heterointerface, altering the position of the heterointerface would inevitably break the constraint of $MoSe_2:WSe_2$ = 1:1. For P_8 with maximum interface density, the periodic length equal to the lattice constant of component orthogonal unit cells. Thus, its all possible hetero-interface locations are fully occupied, leaving no room for further adjustment. Therefore, P_1 and P_8 represent the boundary limits for disordered superlattices.

C. Thermal transport properties

Among MD methods for predicting LTC of 2D materials, the HNEMD method is widely used for its efficiency over other approaches such as equilibrium molecular dynamics (EMD) and non-equilibrium molecular dynamics (NEMD) [20, 44–47]. Therefore, we apply the HNEMD approach (see section IV D for details) to calculate the LTC of $MoSe_2/WSe_2$ lateral heterostructures.

Figure 4 presents the LTC of $MoSe_2/WSe_2$ lateral heterostructures with different interface densities at the room temperature of 300 K. As the interface density increases, the HNEMD-predicted LTC of the perfect superlattice exhibits a non-monotonic trend, first decreasing and then increasing, with a global minimum at P_2 with an interface density of around $0.07\,nm^{-1}$. This behavior reflects the transition of phonon transport from the incoherent to the coherent regime, a phenomenon previously reported in various superlattice systems [5, 6, 8, 9, 12], which can be understood from the
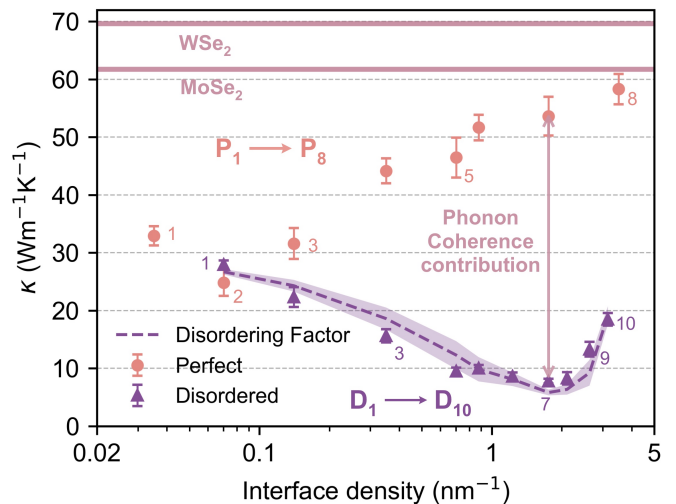

FIG. 4. Thermal conductivity of $MoSe_2/WSe_2$ lateral heterostructures, including perfect ($P_1 \sim P_8$, filled circles) and disordered ($D_1 \sim D_{10}$, filled triangles) superlattices, as a function of interface density at 300 K. The two horizontal solid lines at the top represent the LTC of monolayer $MoSe_2$ and WSe_2, respectively. The dashed line for disordered superlattices corresponds to the disordering factor R-based predictions using Eq. (1) and Eq. (2). Groups marked with numbers will be selected as representative groups for subsequent phonon analysis in Figure 6.

competition between LTC reduction due to enhanced interface scattering and the LTC increase driven by coherent phonon transport. In the incoherent transport regime of low interface density (below $0.07\,nm^{-1}$), the LTC of the perfect superlattice is primarily influenced by interface scattering, with the lower interface density of P_1 resulting in a significantly higher LTC compared to P_2. Conversely, when the interface density is high (above $0.07\,nm^{-1}$), phonon transport of perfect superlattices transitions the coherent regime, resulting in a monotonic increase in LTC with interface density. Notably, at the maximum interface density of $3.51\,nm^{-1}$, the superlattice P_8, with its smallest indivisible unit, reaches a maximum LTC of $58.32\,W/(m\,K)$, approaching that of $MoSe_2$ ($61.75\,W/(m\,K)$) and WSe_2 ($69.65\,W/(m\,K)$), indicating that phonon coherence dominates LTC in this region.

To further understand the phonon coherence observed in perfect superlattices, in Figure 5 we examined the phonon dispersion for P_4, P_6, and P_8 in the coherent transport regime. The clear band folding of acoustic phonons propagating through superlattice is observed here, allowing phonons to propagate in homogeneous materials and free of interfaces. However, this folding introduces two additional stop bands: One is the anti-crossing point, which refers to the intra-mode stop bands generated by the crossing of folded phonon branches with other phonons; another one is the band gap that occurred at
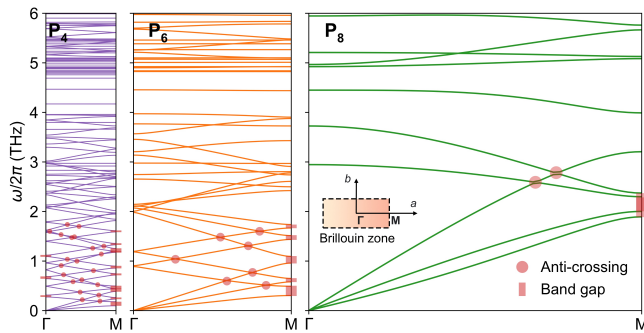
FIG. 5. Phonon dispersion relation of MoSe$_2$/WSe$_2$ lateral superlattice P$_4$, P$_6$, and P$_8$ within the coherent transport regime. The first Brillouin zone is defined by the smallest repeating unit of the superlattice, with the Γ-M direction is along the periodicity of its components, also the thermal transport direction. The phonon dispersion results were calculated by the CALORINE [48] together with PHONOPY packages [49] based on the finite difference method, where the force constants were calculated from the NEP model.

the center and boundary of the folded Brillouin zone. As interface density increases (P4→P8), fewer bands in the perfect superlattice fold, reducing the number of stop bands, which may result in higher group velocity and phonon mean free path (MFP), thereby enhancing the LTC.

In disordered superlattices, phonon coherence is expected to be nearly absent, as shown in previous studies [6, 12]. Thus, the difference in LTC between the perfect and disordered superlattices with identical interface densities reflects the contribution of phonon coherence (see the vertical arrow in Figure 4). In this case, one may intuitively expect the LTC of disordered superlattices to decrease monotonically with increasing interface density due to enhanced interface scattering. However, we observed a similar non-monotonic trend in LTC for disordered superlattices, as seen in perfect superlattices, with the minimum LTC occurring near the maximum interface density limit. This indicates that at very high interface densities (above $1.76\,\mathrm{nm}^{-1}$), wave-like phonons contribute significantly more to LTC than particle-like phonons. We attribute this to the fact that, as the interface density approaches the maximum limit, the disordered superlattice begins to resemble a perfect superlattice, exhibiting a high degree of lagged self-similarity in the structural sequence.

To quantify the lagged self-similarity for disordered superlattices, we can define a disordering factor that measures system disorder using the auto-correlation function of parameterized sequences as follows:

$$R(\tau) = \frac{1}{N-\tau} \sum_{t=0}^{N-\tau-1} \left(x(t) - \mu \right)\left(x(t+\tau) - \mu \right), \quad (1)$$

where τ is the lag parameter, indicating the step number of sequence move backward, and μ is the average of pa-

rameterized sequences. The disordering factor R can be further obtained by considering the average of different lag parameters $R(\tau)$:

$$R = \frac{1}{n} \sum_{\tau=1}^{n} R(\tau), \quad (2)$$

Here we chose $n = 4$ to quantify R. Furthermore, one can predict the LTC using a single scaling factor α and a basis β: $\kappa = \alpha R + \beta$. Remarkably, the $\alpha R + b$ profiles are in excellent agreement with the LTC of disordered superlattices predicted by HNEMD using $\alpha = 20.72\,\mathrm{W/(m\,K)}$ and $\beta = 6.2\,\mathrm{W/(m\,K)}$ (see Figure 4). This strong correlation suggests that the disordering factor serves as a simple and cost-effective predictor for interface density in disordered superlattices with minimum LTC, and can be adapted to describe other aperiodic heterostructures[12].

The LTCs of both perfect and disordered superlattices span a wide range, from approximately $8\,\mathrm{W/(m\,K)}$ to $58\,\mathrm{W/(m\,K)}$. This demonstrates the promising potential for LTC modulation in lateral heterostructures through ordered- or disordered-sequence engineering, particularly as the LTC range of order- and disorder-sequence heterostructures is distinct (see Figure 4).

To gain microscale insights into the interplay between particle-like and wave-like phonons in perfect and disordered superlattices, we spectrally decomposed the LTCs within the HNEMD framework using the spectral heat current decomposition method (see section IV E for details)[44]. Figure 6(a-b) present the spectral LTC ($\kappa(\omega)$) results for perfect (P$_1$, P$_2$, P$_3$, P$_5$, and P$_8$) and disordered superlattices (D$_1$, D$_3$, D$_7$, D$_9$, and D$_{10}$), respectively, each with five representative pairs of perfect and disordered superlattices that have identical interface densities (see Figure 4), effectively capturing the changing trends. For perfect superlattices, the LTCs are primarily contributed by low-frequency in-plane phonons below $4\,\mathrm{THz}$. In the incoherent transport regime (P$_1$→P$_2$), enhanced phonon-interface scattering significantly weakens LTC from low-frequency phonons below $4\,\mathrm{THz}$. Upon entering a coherent transport regime (P$_2$→P$_8$), increasing phonon coherence enables more low-frequency, long-wavelength phonons to participate in transport, primarily concentrated in the in-plane part, also as shown in Figure Figure 6(c). This is in contrast to single-atom-thickness graphene/C$_3$N lateral heterostructure, where the LTC is much higher and dominated by out-of-plane phonon modes [50]. This difference is attributed to the sandwich structure of MoSe$_2$ and WSe$_2$ makes their flexural phonon modes no longer the pure out-of-plane vibration. As a result, the symmetry selection rules are broken, allowing three-phonon scattering processes that involve an odd number of flexural phonons [51].

As shown in Figure 6 (b), the $\kappa(\omega)$ of disordered superlattices, D$_1$ and D$_3$, with low interface density differs significantly from that of perfect superlattices, with peaks appearing around $2\,\mathrm{THz}$, rather than near the $0\,\mathrm{THz}$
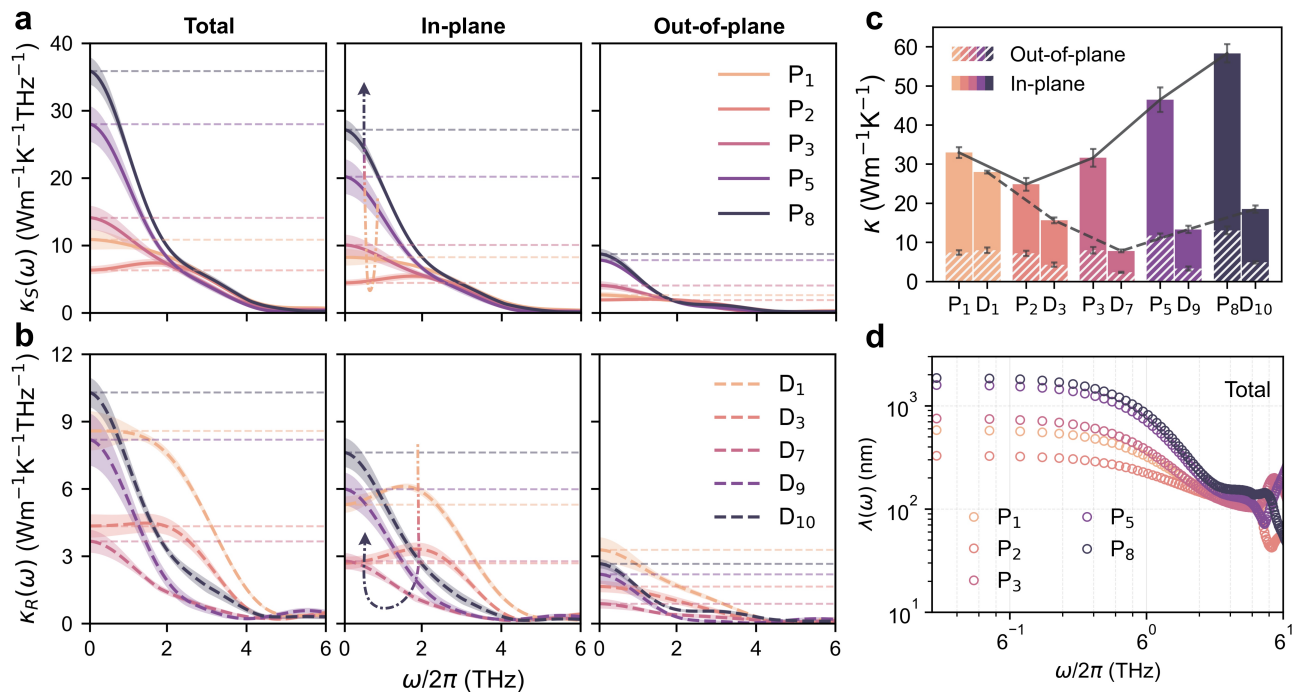
FIG. 6. Spectral LTCs of selected $MoSe_2$/WSe_2 lateral heterostructures. (a-b) Total spectral LTC (left column) and corresponding in-plane (middle column) and out-of-plane (right column) phonon contributions for (a) perfect and (b) disordered superlattices. (c) Comparison of cumulative in-plane and out-of-plane phonon contributions to LTC for each heterostructure. (d) Spectral phonon MFP for five representative structures of the $MoSe_2$/WSe_2 lateral superlattice. In (a-b), the dashed lines with arrows indicate the trend of spectral LTC peak that dominates the LTC with the increasing interface density. The horizontal dashed lines are the reference lines for each $\kappa(\omega)$ value around $0\,THz$. Colored shaded areas represent error bars from multiple independent simulations.

as in superlattices. Compared with D_1, the enhanced phonon-interface scattering in D_3 results in a weakened $\kappa(\omega)$ in the entire frequency range, with peaks attenuated but still present. However, when the interface density increases from around $0.35\,nm^{-1}$ (D_3) to $1.76\,nm^{-1}$ (D_7), the $\kappa(\omega)$ profile undergoes a complete transformation, with the peak shifting towards the $0\,THz$, resembling the peak shape observed in perfect superlattices. As indicated by the dashed arrows labeled in Figure 6(a-b), disordered superlattices show spectral peak shifts that are absent in superlattices. In the high interface density region ($D_7 \rightarrow D_{10}$) where LTC increases with interface density, in-plane phonons below $2\,THz$ dominants the increase and exhibit coherent characteristics similar to those observed in perfect superlattices (also see $P_2 \rightarrow P_8$ in Figure 6(c)). These results suggest that phonon coherence contributes to the increase in LTC in disordered superlattices at high interface densities, as the smaller differences between adjacent units in these configurations facilitate the transmission of low-frequency, long-wavelength wave-like phonons.

As defined in Eq. (8) (see section IV D), one can predict frequency-dependent phonon MFP, $\lambda(\omega)$, using the

following equation:[44]

$$\lambda(\omega) = \frac{\kappa(\omega)}{G(\omega)}, \qquad (3)$$

where $G(\omega)$ is the spectrally thermal conductance in the ballistic regime. Figure 6(d) depicts the $\lambda(\omega)$ profiles for representative perfect superlattices below $6\,THz$, the frequency range that contributes most to LTC. The phonon MFPs align with their LTCs, especially for phonons below $2\,THz$. In the coherent transport regime, enhanced phonon coherence reduces scattering and extends the phonon MFPs. Coherent phonon wave packets maintain their phase relationships, minimizing incoherent scattering, particularly for low-frequency phonons, whose longer wavelengths favor coherent states.

III. SUMMARY AND CONCLUSIONS

In summary, we develop an accurate and efficient machine-learned NEP model for lateral $MoSe_2$/WSe_2 heterostructure, and then perform extensive HNEMD simulations to investigate thermal transport in both perfect and disordered $MoSe_2$/WSe_2 superlattices. Surprisingly, both perfect and disordered superlattices show

a minimum LTC with varying interface density, driven by the transition from incoherent to coherent transport regimes. The counter-intuitive thermal transport behavior of disorder superlattices is well captured by the disordering factor, defined by the auto-correlation function of the parameterized sequence. For the first time, spectral LTC decomposition reveals wave-like low-frequency (long-wavelength) phonons contribute to the increase in LTC of disordered superlattices with high interface densities. We also explained the intrinsic mechanism of coherent phonons enhancing LTC in the perfect superlattices through phonon MFP and stop bands analysis. These findings provide novel physical insights into tuning thermal transport of 2D lateral heterostructures through sequence ordering and disordering, offering a framework applicable to other analogous systems.

IV. METHODS

A. The training dataset

As shown in Figure 1(a), our training dataset consists of nine different configurations, i.e., two pure MX_2 structures ($MoSe_2$ and WSe_2), two $MoSe_2/WSe_2$ heterostructures with the ideal flat interface and mutually embedded interface, and five random ternary transitional $Mo_xW_{1-x}Se$ structures with x increasing from $\frac{1}{6}$ to $\frac{5}{6}$ in increments of $\frac{1}{6}$. For each configuration, we performed constant volume MD simulation driven by the SW potential developed by Jiang et $al.$ [39] for 150 ps with the target temperature linearly increasing from 100 to 800 K and sampled 15 structures. In addition to this, we generated 5 structures by applying random cell deformations (-3 to 3%) and atomic displacements (within 0.1 Å) starting from each initial configuration. In total, we obtained $9 \times (15 + 5) = 180$ structures, which were further randomly divided to a training dataset (150 structures) and a test dataset (30 structures).

B. DFT calculations

To obtain the total energy, atomic forces, and virial for selected structures in the reference dataset, we use the VASP code [52–54] to perform single-point DFT calculations at PBE [55] level. A plane-wave basis set was employed with the energy cutoff of 650 eV and a dense Γ-centered grid with a k-point density of 0.25/Å was sampled in the Brillouin zone. We set a threshold of 10^{-7} eV for the electronic self-consistent loop.

C. NEP model training

Using the provided training and test datasets, we trained the NEP model for the $MoSe_2/WSe_2$ heterosystem with the NEP3 architecture, implemented in GPUMD.[25] The NEP approach [23–25] uses a simple feedforward artificial neural network (ANN) to represent the site energy U_i [56] of atom i as a function of a descriptor vector with N_{des} components:

$$U_i = \sum_{\mu=1}^{N_{neu}} w_\mu^{(1)} \tanh \left(\sum_{\nu=1}^{N_{des}} w_{\mu\nu}^{(0)} q_\nu^i - b_\mu^{(0)} \right) - b^{(1)}, \quad (4)$$

where $\tanh(x)$ is the activation function, $w^{(0)}$, $w^{(1)}$, $b^{(0)}$, and $b^{(1)}$ are the trainable weight and bias parameters in the ANN, and q_ν^i is the descriptor vector constructed similarly to the atomic cluster expansion (ACE) approach [57], but treating radial and angular components separately. Based on the separable natural evolution strategy (SNES) method [58], the optimization of NEP model parameters involves minimizing a loss function that incorporates a weighted sum of the RMSEs for energy, force, and virial, along with regularization terms.

After extensive testing, we determined the following hyper-parameters for NEP training: the cutoffs of radial and angular descriptors were both set to 5 Å and with 8 radial functions. For angular terms, we focused on three-body and four-body interactions, with maximum expansion orders of 4 and 2, respectively. A single hidden layer with 50 neurons was used for the ANN. The optimization was performed with a population size of 50 for 5×10^5 steps. In the loss function, we assigned weights of 1.0 to the RMSEs of energy and force, and 0.1 to the RMSE of virial.

D. The HNEMD method

Based on the linear response theory, the HNEMD method simulates the thermal gradient effect in a solid by applying a directional driving force $\boldsymbol{F}_i^e$ on each atom i [44, 59]:

$$\boldsymbol{F}_i^e = \boldsymbol{F}_e \cdot \mathbf{W}_i, \quad (5)$$

where $\boldsymbol{F}_e$ is the external driving force parameter with the dimension of inverse length, and $\mathbf{W}_i$ is virial tensor of atom i. The running LTC, $\kappa(t)$, along the lateral transport direction can be calculated as:

$$\kappa(t) = \frac{\langle J(t) \rangle_{ne}}{TVF_e}, \quad (6)$$

where k_B is the Boltzmann constant, T is the temperature, V is the volume of the system, and $\langle \boldsymbol{J} \rangle_{ne}$ is non-equilibrium ensemble average of the heat current $\boldsymbol{J} = \sum_i \mathbf{W}_i \cdot \boldsymbol{v}_i$, with $\boldsymbol{v}_i$ being the velocity of atom i. A thickness of 0.65 nm is used to calculate the volume V in Eq. (6) for all structures. To observe the convergence of the calculated LTC results, Eq. (6) can be further redefined as the following cumulative average: $\kappa(t) = \frac{1}{t} \int_0^t \kappa(\tau) d\tau$.

We set the magnitude of the driving force parameter to be $F_e = 1 \times 10^{-5}$/Å along lateral transport directions for

all heterostructures, which is small enough to maintain the linear response regime and is large enough to achieve a sufficiently large signal-to-noise ratio. All heterostructures were set to a length of 56.95 nm along the thermal transport direction, with a width of 9.86 nm and a total of 18,000 atoms. Periodic boundary conditions were applied in both in-plane directions. For the superlattice group, five independent runs were conducted to enhance the statistical accuracy and obtain an error estimate. For the disordered group, three different configurations were created for each interface density, with three independent simulations performed for each configuration. All MD simulations were performed using GPUMD package.[25]. In all MD simulations, the system was first equilibrated at 300 K and zero pressure for 1 ns in the NPT ensemble. In the production stage, the Nose-Hoover chain thermostat [60] was used to maintain the overall temperature and heat current data were collected for 10 ns. A time step of 1 fs was used in all the MD simulations.

E. Spectral heat current decomposition

In the framework of the HNEMD method, one can calculate spectrally decomposed thermal conductivity with the following formula [44]:

$$\kappa = \int_0^\infty \frac{d\omega}{2\pi} \kappa(\omega), \tag{7}$$

where

$$\kappa(\omega) = \frac{2}{VTF_e} \int_{-\infty}^\infty dt e^{i\omega t} K(t). \tag{8}$$

Here, $K(t)$ is the x-component (along lateral direction) of the virial-velocity correlation function [61]:

$$\boldsymbol{K}(t) = \sum_i \langle \mathbf{W}_i(0) \cdot \boldsymbol{v}_i(t) \rangle. \tag{9}$$

For 2D materials considered here, the spectral LTC $\kappa(\omega)$ in Eq. (8) can be further decomposed into in-plane and out-of-plane (flexural) phonon contributions [62].

Conflict of Interest

The authors have no conflicts to disclose.

Data availability

The source code and documentation for GPUMD are available at https://github.com/brucefan1983/GPUMD and https://gpumd.org, respectively. The documentation for CALORINE is available at https://calorine.materialsmodeling.org. The documentation for PHONOPY is available at https://phonopy.github.io/phonopy/. The inputs and outputs related to the NEP model training are freely available at the Gitlab repository https://gitlab.com/brucefan1983/nep-data.

[1] Gang Chen, *Nanoscale Energy Transport and Conversion: A Parallel Treatment of Electrons, Molecules, Phonons, and Photons* (Oxford University Press, 2005).

[2] Zhongwei Zhang, Yangyu Guo, Marc Bescond, Jie Chen, Masahiro Nomura, and Sebastian Volz, "How coherence is governing diffuson heat transfer in amorphous solids," npj Computational Materials **8**, 96 (2022,12).

[3] Zhongwei Zhang, Yangyu Guo, Marc Bescond, Jie Chen, Masahiro Nomura, and Sebastian Volz, "Generalized decay law for particlelike and wavelike thermal phonons," Physical Review B **103**, 184307 (2021).

[4] S. Tamura, D. C. Hurley, and J. P. Wolfe, "Acoustic-phonon propagation in superlattices," Physical Review B **38**, 1427–1449 (1988).

[5] M. V. Simkin and G. D. Mahan, "Minimum thermal conductivity of superlattices," Physical Review Letters **84**, 927–930 (2000).

[6] Maria N. Luckyanova, Jivtesh Garg, Keivan Esfarjani, Adam Jandl, Mayank T. Bulsara, Aaron J. Schmidt, Austin J. Minnich, Shuo Chen, Mildred S. Dresselhaus, Zhifeng Ren, Eugene A. Fitzgerald, and Gang Chen, "Coherent phonon heat conduction in superlattices," Science **338**, 936–939 (2012).

[7] B. Latour, S. Volz, and Y. Chalopin, "Microscopic description of thermal-phonon coherence: From coherent transport to diffuse interface scattering in superlattices," Physical Review B **90**, 014307 (2014).

[8] Isaac M. Felix and Luiz Felipe C. Pereira, "Thermal conductivity of graphene-hbn superlattice ribbons," Scientific Reports **8**, 2737 (2018).

[9] Xin Wu and Qiang Han, "Transition from incoherent to coherent phonon thermal transport across graphene/h-bn van der waals superlattices," International Journal of Heat and Mass Transfer **184**, 122390 (2022).

[10] Masahiro Nomura, Roman Anufriev, Zhongwei Zhang, Jeremie Maire, Yangyu Guo, Ryoto Yanagisawa, and Sebastian Volz, "Review of thermal transport in phononic crystals," Materials Today Physics **22**, 100613 (2022).

[11] C. Colvard, T. A. Gant, M. V. Klein, R. Merlin, R. Fischer, H. Morkoc, and A. C. Gossard, "Folded acoustic and quantized optic phonons in (gaal)as superlattices," Physical Review B **31**, 2080–2091 (1985).

[12] Run Hu, Sotaro Iwamoto, Lei Feng, Shenghong Ju, Shiqian Hu, Masato Ohnishi, Naomi Nagai, Kazuhiko Hirakawa, and Junichiro Shiomi, "Machine-learning-optimized aperiodic superlattice minimizes coherent phonon heat conduction," Physical Review X **10**, 021050 (2020).

[13] Yan Wang, Haoxiang Huang, and Xiulin Ruan, "Decomposition of coherent and incoherent phonon conduction in superlattices and random multilayers," Physical Review B **90**, 165406 (2014).

[14] Han Wei, Yue Hu, Hua Bao, and Xiulin Ruan, "Quantifying the diverse wave effects in thermal transport of nanoporous graphene," Carbon **197**, 18–26 (2022).

[15] Zhang Wu, Rumeng Liu, Ning Wei, and Lifeng Wang, "Unexpected reduction in thermal conductivity observed in graphene/h-bn heterostructures," Physical Chemistry Chemical Physics **26**, 3823–3831 (2024).

[16] Hua Bao, Jie Chen, Xiaokun Gu, and Bingyang Cao, "A review of simulation methods in micro/nanoscale heat conduction," ES Energy & Environment (2018), 10.30919/esee8c149.

[17] Jörg Behler, "Perspective: Machine learning potentials for atomistic simulations," The Journal of Chemical Physics **145**, 170901 (2016).

[18] Yanzhou Wang, Zheyong Fan, Ping Qian, Miguel A. Caro, and Tapio Ala-Nissila, "Quantum-corrected thickness-dependent thermal conductivity in amorphous silicon predicted by machine learning molecular dynamics simulations," Physical Review B **107**, 054303 (2023).

[19] Ting Liang, Penghua Ying, Ke Xu, Zhenqiang Ye, Chao Ling, Zheyong Fan, and Jianbin Xu, "Mechanisms of temperature-dependent thermal transport in amorphous silica from machine-learning molecular dynamics," Physical Review B **108**, 184203 (2023).

[20] Penghua Ying, Ting Liang, Ke Xu, Jin Zhang, Jianbin Xu, Zheng Zhong, and Zheyong Fan, "Sub-micrometer phonon mean free paths in metal–organic frameworks revealed by machine learning molecular dynamics simulations," ACS Applied Materials & Interfaces **15**, 36412–36422 (2023).

[21] Ke Xu, Yongchao Hao, Ting Liang, Penghua Ying, Jianbin Xu, Jianyang Wu, and Zheyong Fan, "Accurate prediction of heat conductivity of water by a neuroevolution potential," The Journal of Chemical Physics **158**, 204114 (2023).

[22] Haikuan Dong, Yongbo Shi, Penghua Ying, Ke Xu, Ting Liang, Yanzhou Wang, Zezhu Zeng, Xin Wu, Wenjiang Zhou, Shiyun Xiong, Shunda Chen, and Zheyong Fan, "Molecular dynamics simulations of heat transport using machine-learned potentials: A mini-review and tutorial on gpumd with neuroevolution potentials," Journal of Applied Physics **135**, 161101 (2024).

[23] Zheyong Fan, Zezhu Zeng, Cunzhi Zhang, Yanzhou Wang, Keke Song, Haikuan Dong, Yue Chen, and Tapio Ala-Nissila, "Neuroevolution machine learning potentials: Combining high accuracy and low cost in atomistic

simulations and application to heat transport," Physical Review B **104**, 104309 (2021).

[24] Zheyong Fan, "Improving the accuracy of the neuroevolution machine learning potential for multi-component systems," Journal of Physics: Condensed Matter **34**, 125902 (2022).

[25] Zheyong Fan, Yanzhou Wang, Penghua Ying, Keke Song, Junjie Wang, Yong Wang, Zezhu Zeng, Ke Xu, Eric Lindgren, J. Magnus Rahm, Alexander J. Gabourie, Jiahui Liu, Haikuan Dong, Jianyang Wu, Yue Chen, Zheng Zhong, Jian Sun, Paul Erhart, Yanjing Su, and Tapio Ala-Nissila, "Gpumd: A package for constructing accurate machine-learned potentials and performing highly efficient atomistic simulations," The Journal of Chemical Physics **157**, 114801 (2022).

[26] Puqing Jiang, Xin Qian, Xiaokun Gu, and Ronggui Yang, "Probing anisotropic thermal conductivity of transition metal dichalcogenides mx2 (m = mo, w and x = s, se) using time-domain thermoreflectance," Advanced Materials **29**, 1701068 (2017).

[27] Xian Zhang, Dezheng Sun, Yilei Li, Gwan-Hyoung Lee, Xu Cui, Daniel Chenet, Yumeng You, Tony F. Heinz, and James C. Hone, "Measurement of lateral and interfacial thermal conductivity of single- and bilayer mos2 and mose2 using refined optothermal raman technique," ACS Applied Materials & Interfaces **7**, 25923–25929 (2015).

[28] Yifei Yu, Tamzid Minhaj, Lujun Huang, Yiling Yu, and Linyou Cao, "In-plane and interfacial thermal conduction of two-dimensional transition-metal dichalcogenides," Physical Review Applied **13**, 034059 (2020).

[29] Elham Easy, Yuan Gao, Yingtao Wang, Dingkai Yan, Seyed M. Goushehgir, Eui-Hyeok Yang, Baoxing Xu, and Xian Zhang, "Experimental and computational investigation of layer-dependent thermal conductivities and interfacial thermal conductance of one- to three-layer wse2," ACS Applied Materials & Interfaces **13**, 13063–13071 (2021).

[30] Xiaokun Gu and Ronggui Yang, "Phonon transport in single-layer transition metal dichalcogenides: A first-principles study," Applied Physics Letters **105**, 131903 (2014).

[31] Bo Peng, Hao Zhang, Hezhu Shao, Yuchen Xu, Xiangchao Zhang, and Heyuan Zhu, "Thermal conductivity of monolayer mos $_2$, mose $_2$, and ws $_2$: Interplay of mass effect, interatomic bonding and anharmonicity," RSC Advances **6**, 5767–5773 (2016).

[32] Roberta Farris, Olle Hellman, Zeila Zanolli, David Saleta Reig, Sebin Varghese, Pablo Ordejón, Klaas-Jan Tielrooij, and Matthieu Jean Verstraete, "Microscopic understanding of the in-plane thermal transport properties of 2 h transition metal dichalcogenides," Physical Review B **109**, 125422 (2024).

[33] Kunpeng Yuan, Xiaoliang Zhang, Lin Li, and Dawei Tang, "Effects of tensile strain and finite size on thermal conductivity in monolayer wse2," Physical Chemistry Chemical Physics **21**, 468–477 (2018).

[34] Yingtao Wang and Xian Zhang, "On the role of crystal defects on the lattice thermal conductivity of monolayer wse2 (p63/mmc) thermoelectric materials by dft calculation," Superlattices and Microstructures **160**, 107057 (2021).

[35] Yang Hong, Jingchao Zhang, and Xiao Cheng Zeng, "Thermal conductivity of monolayer mose2 and mos2," The Journal of Physical Chemistry C **120**, 26067–26075

(2016).

[36] Ali Kandemir, Haluk Yapicioglu, Alper Kinaci, Tahir Çağın, and Cem Sevik, "Thermal transport properties of mos $_2$ and mose $_2$ monolayers," Nanotechnology **27**, 055703 (2016).

[37] Jingchao Zhang, Yang Hong, Xinyu Wang, Yanan Yue, Danmei Xie, Jin Jiang, Yangheng Xiong, and Peisheng Li, "Phonon thermal properties of transition-metal dichalcogenides mos $_2$ and mose $_2$ heterostructure," The Journal of Physical Chemistry C **121**, 10336–10344 (2017).

[38] Arash Mobaraki, Cem Sevik, Haluk Yapicioglu, Deniz Çakır, and Oğuz Gülseren, "Temperature-dependent phonon spectrum of transition metal dichalcogenides calculated from the spectral energy density: Lattice thermal conductivity as an application," Physical Review B **100**, 035402 (2019).

[39] Jin-Wu Jiang, "Misfit strain-induced buckling for transition-metal dichalcogenide lateral heterostructures: A molecular dynamics study," Acta Mechanica Solida Sinica **32**, 17–28 (2019).

[40] Aidan P. Thompson, H. Metin Aktulga, Richard Berger, Dan S. Bolintineanu, W. Michael Brown, Paul S. Crozier, Pieter J. in 't Veld, Axel Kohlmeyer, Stan G. Moore, Trung Dac Nguyen, Ray Shan, Mark J. Stevens, Julien Tranchida, Christian Trott, and Steven J. Plimpton, "LAMMPS-A Flexible Simulation Tool for Particle-Based Materials Modeling at the Atomic, Meso, and Continuum Scales," Computer Physics Communications **271**, 108171 (2022).

[41] Jinwu Jiang and Yuping Zhou, eds., Handbook of Stillinger-Weber Potential Parameters for Two-Dimensional Atomic Crystals (InTech, 2017).

[42] Yufeng Zhang, Qian Lv, Haidong Wang, Shuaiyi Zhao, Qihua Xiong, Ruitao Lv, and Xing Zhang, "Simultaneous electrical and thermal rectification in a monolayer lateral heterojunction," Science **378**, 169–175 (2022).

[43] Darrell Whitley, "A genetic algorithm tutorial," Statistics and computing **4**, 65–85 (1994).

[44] Zheyong Fan, Haikuan Dong, Ari Harju, and Tapio Ala-Nissila, "Homogeneous nonequilibrium molecular dynamics method for heat transport and spectral decomposition with many-body potentials," Physical Review B **99**, 064308 (2019).

[45] Xiaokun Gu, Zheyong Fan, and Hua Bao, "Thermal conductivity prediction by atomistic simulation methods: Recent advances and detailed comparison," Journal of Applied Physics **130**, 210902 (2021).

[46] Xin Wu and Qiang Han, "Thermal transport in pristine and defective two-dimensional polyaniline (c3n)," International Journal of Heat and Mass Transfer **173**, 121235 (2021).

[47] Haikuan Dong, Yongbo Shi, Penghua Ying, Ke Xu, Ting Liang, Yanzhou Wang, Zezhu Zeng, Xin Wu, Wenjiang Zhou, Shiyun Xiong, et al., "Molecular dynamics simulations of heat transport using machine-learned potentials: A mini-review and tutorial on gpumd with neuroevolution potentials," Journal of Applied Physics **135**, 161101

[48] Eric Lindgren, Magnus Rahm, Erik Fransson, Fredrik Eriksson, Nicklas Österbacka, Zheyong Fan, and Paul Erhart, "Calorine: A python package for constructing and sampling neuroevolution potential models," Journal of Open Source Software **9**, 6264 (2024).

[49] Atsushi Togo, "First-principles phonon calculations with phonopy and phono3py," Journal of the Physical Society of Japan **92**, 012001 (2023).

[50] Xin Wu, Penghua Ying, Chunlei Li, and Qiang Han, "Dual effects of hetero-interfaces on phonon thermal transport across graphene/c3n lateral superlattices," International Journal of Heat and Mass Transfer **201**, 123643 (2023).

[51] Xiaokun Gu, Yujie Wei, Xiaobo Yin, Baowen Li, and Ronggui Yang, "*Colloquium*: Phononic thermal properties of two-dimensional materials," Reviews of Modern Physics **90**, 041002 (2018).

[52] Georg Kresse and Jürgen Furthmüller, "Efficiency of ab-initio total energy calculations for metals and semiconductors using a plane-wave basis set," Computational materials science **6**, 15–50 (1996).

[53] Georg Kresse and Jürgen Furthmüller, "Efficient Iterative Schemes for Ab Initio Total-Energy Calculations Using a Plane-Wave Basis Set," Physical Review B **54**, 11169 (1996).

[54] Georg Kresse and Daniel Joubert, "From Ultrasoft Pseudopotentials to the Projector Augmented-Wave Method," Physical Review B **59**, 1758 (1999).

[55] Peter E Blöchl, "Projector augmented-wave method," Physical review B **50**, 17953 (1994).

[56] Jörg Behler and Michele Parrinello, "Generalized Neural-Network Representation of High-Dimensional Potential-Energy Surfaces," Physical Review Letters **98**, 146401 (2007).

[57] Ralf Drautz, "Atomic cluster expansion for accurate and transferable interatomic potentials," Physical Review B **99**, 014104 (2019).

[58] Tom Schaul, Tobias Glasmachers, and Jürgen Schmidhuber, "High Dimensions and Heavy Tails for Natural Evolution Strategies," in Proceedings of the 13th Annual Conference on Genetic and Evolutionary Computation, GECCO '11 (Association for Computing Machinery, New York, NY, USA, 2011) pp. 845–852.

[59] Denis J. Evans, "Homogeneous nemd algorithm for thermal conductivity—application of non-canonical linear response theory," Physics Letters A **91**, 457–460 (1982).

[60] Mark E Tuckerman, Statistical mechanics: theory and molecular simulation (Oxford university press, 2023).

[61] Alexander J Gabourie, Zheyong Fan, Tapio Ala-Nissila, and Eric Pop, "Spectral decomposition of thermal conductivity: Comparing velocity decomposition methods in homogeneous molecular dynamics simulations," Physical Review B **103**, 205421 (2021).

[62] Zheyong Fan, Luiz Felipe C Pereira, Petri Hirvonen, Mikko M Ervasti, Ken R Elder, Davide Donadio, Tapio Ala-Nissila, and Ari Harju, "Thermal conductivity decomposition in two-dimensional materials: Application to graphene," Physical Review B **95**, 144309 (2017).